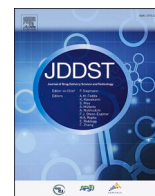




Contents lists available at ScienceDirect

Journal of Drug Delivery Science and Technology

journal homepage: www.elsevier.com/locate/jddst

Transdermal delivery of insulin across human skin *in vitro* with 3D printed hollow microneedles

Iakovos Xenikakis^a, Konstantinos Tsongas^b, Emmanouil K. Tzimtzimis^b, Orestis L. Katsamenis^c, Efterpi Demiri^d, Constantinos K. Zacharis^e, Despoina Georgiou^f, Eleni P. Kalogianni^f, Dimitrios Tzetzis^{b,**}, Dimitrios G. Fatouros^{a,*}

^a Department of Pharmacy, Division of Pharmaceutical Technology, Aristotle University of Thessaloniki, Thessaloniki, 54124, Greece

^b Digital Manufacturing and Materials Characterization Laboratory, School of Science and Technology, International Hellenic University, 14km Thessaloniki - N. Moudania, Themi, GR57001, Greece

^c μ -VIS X-Ray Imaging Centre, Faculty of Engineering and Physical Sciences, University of Southampton, SO17 1BJ, Southampton, UK

^d Department of Plastic Surgery, Medical School, Papageorgiou Hospital, Aristotle University of Thessaloniki, Thessaloniki, Greece

^e Laboratory of Pharmaceutical Analysis, Department of Pharmaceutical Technology, School of Pharmacy, Aristotle University of Thessaloniki, GR-54124, Greece

^f Department of Food Science and Technology, International Hellenic University, Sindos Campus, 57400, Thessaloniki, Greece

ARTICLE INFO

Keywords:

3D printed hollow microneedles
Insulin
Transdermal delivery

ABSTRACT

In the current study hollow microneedles (HMNs) were fabricated by means of vat polymerization method for the transdermal delivery of insulin. Two geometries of HMNs were designed in a Computer Aided Design (CAD) software namely, curved pyramid and syringe-like and fabricated with Liquid Crystal Display (LCD) method. Dimensions were determined and quality features were imaged with scanning electron microscopy (SEM). Volumetric characterization of HMNs and microchannels was performed by microfocus computed tomography (μ CT) whereas mechanical characterization and skin penetration tests of the two geometries were carried out both experimentally and by Finite Element Analysis (FEA) simulation. Diffusion studies of insulin across full thickness human skin were performed *in vitro* using Franz diffusion cells. Insulin samples were analyzed with liquid chromatography-mass spectrometry (LC-MS). The results show that the transport might be affected by the shape of the microneedles.

1. Introduction

Diabetes mellitus is an endocrine pancreatic disorder which impairs glucose metabolism resulting in increased glucose blood levels. In many cases insulin replacement therapy is mandatory for managing the disorder and improving tissue glucose uptake. Insulin administration takes place exclusively through parenteral route [1,2]. This restriction results from the peptide's nature, which makes the specific and other protein drugs vulnerable to enzymatic degradation and extreme pH conditions of oral route [3]. Hence, insulin delivery in the current clinical praxis is performed with syringe equipment, which is associated with pain, patient anxiety and non-compliance to therapeutic treatment [4]. To deal with this issue, scientific research has focused on alternative methods with the aim of making delivery of macromolecular drugs more patient friendly. These methods enhance transdermal delivery and include use

of liposomes [5], nanoparticles [6], jet injectors [7] and electrical assisted methods such as sonophoresis [8], electroporation [9] and iontophoresis [10]. Additionally, use of microneedles (MNs) has been under intensive research over the last two decades. MNs are miniature devices containing micron sized needles ($\leq 1000 \mu\text{m}$) which facilitate transdermal delivery causing perforation of stratum corneum (SC) when applied on skin. Subsequently, pharmaceutical cargo is released in the deeper layers of skin until it reaches systemic circulation. Compared with other enhancing technics, MNs provide a more efficient drug pathway due to the large pores created after application. Moreover, they enable self-administration and minimize pain sensation, while improving thermostability of drug formulations [11,12]. Among the different types of microneedles, HMNs have been used for insulin administration [13–17]. 3D printing of HMNs has been conducted mainly by means of Two Photon Polymerization (2-TPP) [18–24], which

* Corresponding author.

** Corresponding author.

E-mail addresses: d.tzetzis@ihu.edu.gr (D. Tzetzis), dfatouro@pharm.auth.gr (D.G. Fatouros).

<https://doi.org/10.1016/j.jddst.2021.102891>

Received 15 June 2021; Received in revised form 21 September 2021; Accepted 28 September 2021

Available online 20 October 2021

1773-2247/© 2021 Elsevier B.V. All rights reserved.

is one of the most accurate but also expensive methods in 3D-printing technology [25]. In addition, HMNs have been manufactured using stereolithography (SLA) [26,27], while Miller et al. fabricated HMNs with the aid of a digital micromirror device system intending to transdermal electrochemical sensing [28]. HMN fabrication using Fused Deposition Modelling and Selective Laser μ -Melting have also been referred [29,30]. Recently, during 2021, the first research concerning stereolithographic 3D printing of HMNs and *in vivo* insulin delivery was published by Economidou et al. [31] The same research team had previously demonstrated *in vivo* insulin delivery to diabetic rats using SLA printed microneedles, inkjet printed with insulin formulations [32].

In the current study, HMNs differing in shape (curved pyramid vs syringe-like), were manufactured by Liquid Crystal Display (LCD) vat polymerization and evaluated as a mean for the transdermal delivery of insulin *in vitro*. Vat polymerization methods (VPMs such as TPP, SLA and Digital Light Processing or DLP) offer the high accuracy needed for complicated microstructures such as HMNs. Among VPMs, LCD, an unexploited printing method in pharmaceutical technology, is distinguished due to the fact that satisfying resolutions (50 μ m at vertical direction) are combined with low costs, favoring thus large scale production of high complexity objects [33]. LCD method prints typically faster than stereolithography (SLA) which has been recently used for HMN fabrication, as each layer is flashed and subsequently polymerized at once and not as a single point. Additionally, LCD method includes curing process in the printing procedure, while in SLA curing process is conducted with extra equipment as a post printing procedure. Moreover, in LCD method the resin tank is continuously illuminated with LED sources, while LCD screen determines the sites of polymerization and the final quality product according to the number of pixels included. Quality product can be easily improved replacing LCD screen with an upgraded version, extending laboratory life of LCD 3D-printers.

After fabrication procedure, LCD printed HMNs were assessed for their structural characteristics by means of SEM and X-ray μ CT. The mechanical strength of the microneedles was also assessed, while skin penetration studies across human skin *ex vivo* were conducted. Finally, permeation studies of insulin across human skin *in vitro* were performed using Franz cells followed by quantification of insulin by means of LC-MS, whereas the effect of geometry of HMNs on insulin delivery was evaluated. The present research contributes to pharmaceutical science, as insulin is delivered *in vitro* across full-thickness human skin, which poses a more realistic biological barrier over commonly used animal tissues. In addition, LCD method has not been used by other research groups whereas transdermal insulin delivery with use of 3D printed HMNs is sparsely referred in literature [31,34].

2. Materials and methods

2.1. Materials

NextDent Ortho Rigid resin (NextDent B.V., Netherlands) was purchased from Dentalcom Papazoglou S.A. (Greece). Absolute ethanol ($\geq 98\%$, GC), Pluronic F-127, disodium hydrogen phosphate dodecahydrate ($\text{Na}_2\text{HPO}_4 \cdot 12\text{H}_2\text{O}$), potassium dihydrogen phosphate (KH_2PO_4), sodium chloride (NaCl), potassium chloride (KCl), disodium hydrogen phosphate dihydrate ($\text{Na}_2\text{HPO}_4 \cdot 2\text{H}_2\text{O}$), citrate acid monohydrate (MW 210Da) and human insulin (MW 5808Da) were purchased from Sigma Aldrich (St Louis MO, USA). Methanol (LC-MS grade) was obtained by VWR chemicals (Vienna, Austria), while formic acid (99–100%) was supplied by Sigma-Aldrich (St. Louis, MO, USA). High-purity water (18.2 M Ω cm resistivity) was produced by a B30 water purification system (Adrona SIA, Riga, Latvia).

2.2. Design and fabrication

HMN arrays (6 \times 6) were designed with two different geometries namely curved pyramid and syringe-like, using a SolidWorks CAD

software (Dassault Systèmes, SolidWorks Corporation, Waltham, MA, USA). Height was set around 1000 μ m, while interspacing was 2000 μ m (center to center distance). The whole patch was a 15 \times 15 mm square surface. 3D-printing was conducted with Phrozen Shuffle 2018 3D printer, which polymerizes utilizing a LED light source. Resin NextDent Ortho Rigid, a biocompatible resin (Class IIa) was used as printing material. Final printing parameters were adjusted with ChiTuBox 64 slicing software. Printing angle varied depending on geometry; for curved pyramid was 52.63°, whereas for syringe-like was 36.25°, with the aim of making the HMN surface containing the channel projection, parallel to the building platform. Curing time was set at 70s for the first 12 layers (burn-in layers) and 8s for the rest whereas printing resolution was 100 μ m for the burn-in layers and 30 μ m for the rest of the part.

Reservoirs suitable for HMN attachment were fabricated with the upper internal square perimeter slightly larger than HMNs' (15.2 \times 15.2 mm). Reservoirs resembled a funnel shaped inner space, which inscribes all microchannels of the array on the one side allowing tube fitting on the other side. 3D printed fabricated HMN arrays and reservoirs were immersed in isopropyl alcohol solution for 3min under ultrasonic application (Hielscher UP200s, Teltow, Germany). Amplitude of ultrasonic processor was 35%, whereas pulse around 40%. Next, printlets were immersed in a clean alcoholic solution for another 2 min and finally they were dried in an air circulated oven (Binder FD56, Tuttlinger, Germany) for 20 min at 25 °C.

2.3. Scanning electron microscopy (SEM) studies

The structural features and the dimensions of HMN arrays were determined by of SEM studies. HMNs were inserted in a charge reduction sample holder and visualized with a Desktop Phenom ProX scanning electron microscope (ThermoFischer, USA).

2.4. X-ray μ CT studies

2.4.1. Equipment & acquisition

Volumetric characterisation of the printed product was conducted by means of μ CT. Samples were imaged using an in house designed X-ray histology (www.xrayhistology.org) μ CT scanner build on the back of a Nikon XTH225ST system. The experiments took place at the μ -VIS/Biomedical Imaging Unit joined facilities at the University hospital Southampton. Imaging conditions were selected so that a minimum of 10% transmission of the incoming X-ray beam was maintained at all exposure angles during the 360° rotation of the specimen. The scans were conducted at a peak voltage of 80 kVp and a power of 8.8 W (current: 110 μ A) using a tungsten (W) target. The 2850 \times 2850 pixels detector was used un-binned, and the source-to-detector and source-to-object distances were set to 1132.1 mm and 68 mm respectively, resulting in a pixel size of 9 μ m (geometric magnification:16.65).

Imaging parameters were as follows: 3001 projections were taken over the 360° rotation, with 4 frames per projection being averaged to improve the signal to noise ratio. Exposure time of each projection was 177 ms and the detector's gain was set to 30 dB.

2.4.2. Reconstruction, visualization and analysis

After CT acquisition, the data were reconstructed into 32-bit volume files by means of Nikon's own reconstruction software, which uses a filtered-back projection algorithm. The reconstructed 32-bit raw image volumes were then converted to 8-bit volumes for visualization and quantification. Volume segmentation and quantification was conducted in Dragonfly (v. 2021.1.0.977; Object Research Systems (ORS) Inc, Montreal CA). The analysis was focused on the central 16 (4 \times 4) needles of the patch to ensure that no edge-imaging artefacts would interfere with the analysis.

For the analysis each volume was "split" in two along the Z-axis, resulting into two sub-volumes: one containing the protruding needles and the other one their lumen. This allowed us to conduct the most

relevant analysis for each of these two features. Following thresholding-based segmentation, each needle and each lumen was analyzed independently and the following measured were calculated: *Volume* (mm³), *Volume/Surface Area* (mm), *Maximum Location Z* (mm) - *Maximum Location Z* (mm), *Aspect Ratio* and *Minimum Ferret Diameter* (mm). Interpretation of these measures is discussed below in more detail.

2.5. Contact angle goniometry studies

Microneedles were coated with 5% w/v solution of Pluronic F-127 to ensure free passage of the aqueous solution of the macromolecule. Briefly, microneedles were immersed into an ethanolic solution of the polymer for 30min and subsequently dried for 5–10min into an oven at 50 °C (Binder FD56, Tuttlinger, Germany). This was repeated four times, aiming to enhance the hydrophilic character of the microchannel walls.

In order to determine the successful addition of the polymer, goniometry studies were carried out using the drop shape method. First, films 15 mm × 15 mm were 3D-printed with printing angles being the same with those used at microneedle printings (36.25°, 52.63°). Films were coated with polymer according to the procedure described above. A triplet of coated films was further water rinsed (1 mL ultrapure, Milli-Q) to investigate if polymer is removed. Next, contact angles were measured by CAM200 (KSV) at 25 °C. For this a microdroplet was formed with the aid of a needle-gastight syringe- (Hammilton) – pumping system (KSV) on the surface of coated and uncoated substrates. Microdroplets were formed at several points of each 3D-printed film to examine possible heterogeneities within the films. Measurements were taken at all available samples. Measurements were taken every 5 s in order to examine possible gradual wetting behavior and lasted until an equilibrium contact angle was reached. For the present samples equilibrium was reached at times below 20 s. Given the structured surface of the material preliminary measurements were also performed in order to observe possible pinning of the water droplet on several points of the structured surface that would affect the wetting behavior. These measurements were performed both by gradually increasing the water droplet and observing the time dependence of the contact line as well as observing the position of the contact line as a function of time during evaporation. No pinning was observed in any of the examined material at the scale of examination. One-Attension software (version 1.8 Biolin Scientific) was used for contact angle determination and drop shape analysis.

2.6. Mechanical characterization

Mechanical characterization was conducted using a tensile test machine equipped with a 500 N load cell (M500-50AT Testometric Company, Rochdale, UK). HMNs were mounted on a steel plate with double sided adhesive tape. A metal rod located above the steel plate, was programmed to descend at the rate of 0.5 mm/min causing compression failure of HMN arrays with forces up to 650 N. This procedure was repeated for at least 3 HMN arrays per geometry. Prior and after experiment, SEM images were acquired and examined for possible alterations of HMNs.

2.7. Skin penetration test

Skin samples were obtained from female donors (average age 51 ± 4 years old) who had been subjected to cosmetic surgery operation. Samples were immediately transferred to laboratory and pinned on Styrofoam. Fatty tissue was removed using scalpels. Skin samples were immediately used in experimental procedures after being cleaned with water impregnated cotton. Samples were obtained from at least three different donors. Skin penetration test was carried out with the tensile machine used for compression test. First, a 500 µm thickness dental wax sheet was placed on a wooden substrate and skin samples were transferred and stretched on top of them with dermis side down [35]. The

skin assembly was next placed on the steel plate of the tensile machine. HMN arrays of both geometries were fastened on the metal rod with double sided adhesive tape, facing skin samples. The rod was adjusted to descend at 0.5 mm/min, so that HMNs be applied on stratum corneum pressing the underlying skin layers with forces up to 5 N and 10 N, depending on the geometrical configuration of the HMNs. After loading, these ultimate forces were kept constant for 1min. A force-displacement curve was recorded and at the end of the experiment skin samples were inspected with optical microscope to locate the microneedle created perforation sites. Experimental procedure was conducted in duplicate per geometry.

2.8. Skin visualization studies

Skin samples were heated for 2min at 60 °C and epidermis layers were removed using blunt forceps. Epidermis samples were placed on PBS soaked filter paper which was previously placed on cork dishes. HMN treatment followed as referred at permeability studies. Epidermis was fixed with 10% formaldehyde solution for 10 min. Subsequently, epidermis samples were placed in alcoholic solutions of increasing concentrations namely 50, 70, 96 and 100%, for 30min in each case. After all, samples were taken at dehydrated condition and attached on metal stubs using carbon tape. A 90 nm gold layer was coated with a sputter coater (Quorum, UK). Finally, samples were inserted in SEM microscope and thoroughly inspected.

2.9. Diffusion studies

2.9.1. Insulin stability and absorption studies

Aliquots of 4 mL of 20 U/mL insulin solution (citrate-phosphate buffer) was kept at 37 °C for 60 min. At 60 min a volume of 1 mL was collected and further analyzed by LC-MS. Any absorption of insulin to microneedles was evaluated by mounting 3D printed films of 1 cm² surface between side-by-side Franz cells using dental wax. Franz cells were filled with 3 mL of 20 U/mL insulin solution which were in contact with the 3D printed films. At 2 min, aliquots of 1 mL were taken and analyzed. All experiments were carried out in triplicate.

2.9.2. In vitro permeation studies

Permeation studies were conducted using vertical Franz diffusion cells and human insulin. HMN devices (HMNs of different geometries assembled with reservoirs) were manually pressed against skin samples for at least 30s exerting periodically soothe vibrating moves. Skin samples had been placed on a dental wax covered wooden substrate, according to skin penetration procedure. Subsequently, skin tissues along with HMN devices were transferred on Franz receptors and donors were fastened. Franz receptors contained Phosphate Buffer Saline (PBS), pH 7.4.

Next, using a Watson-Marlow 205CA pump, insulin solution (1 mL, 20 IU/mL in citrate-phosphate buffer) was pumped at a flow rate of 0.5 mL/min through HMN devices, according to the set-up being presented in Fig. 1. HMN devices were accompanied with pump tubing from the beginning of the experiment. After HMN device-Franz cell set up, tubing related to Watson-Marlow pump. At the end of the administration, pump and HMN devices were removed, and donors were covered with parafilm. At 60 min, sample aliquots of 1 mL were collected from the receptors and then analyzed by liquid chromatography-mass spectrometry (LC-MS).

2.10. Peptide quantification by LC-MS

Method validation and insulin sample analyses were performed using an Acquity UPLC binary solvent system (Waters) coupled to a TDQ triple quadrupole MS/MS (Waters). Chromatographic separations were achieved on a Poroshell EC-C18 120 (50 × 4.6 mm, 2.7 µm, Agilent Technologies) thermostated at 40 °C. The autosampler temperature was

3D printed assembly of the microfluidic device

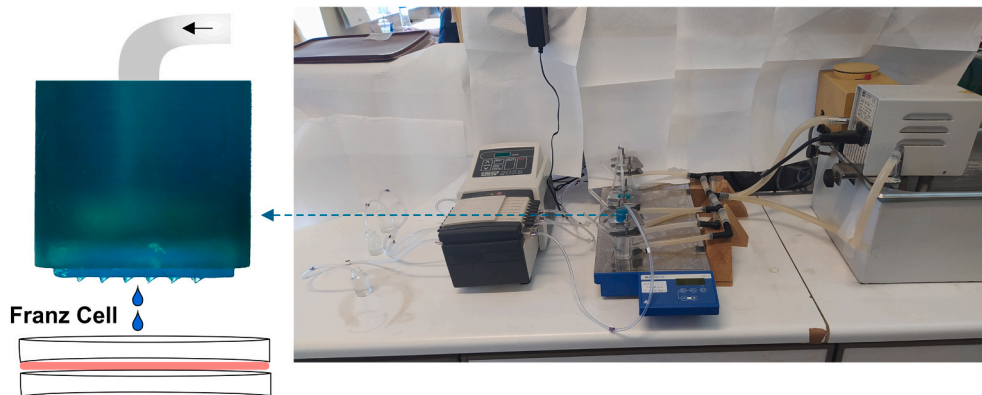


Fig. 1. Capture of a HMN loaded Franz cell along with the pump used in diffusion studies. At the left side, a detailed schematic showing how the whole set up performs.

set at 10 °C. The mobile phase consisted of water (A) and methanol (B) both acidified with 0.1% v/v formic acid. The flow rate and the injection volume were set at 0.5 mL/min and 5 μ L, respectively. At the beginning of the gradient elution, the composition was 10% B and kept constant for 1 min and was linearly increased to 90% B in 3 min and then was altered to the initial ratio of 10% B at 3.5 min and kept constant up to 6 min for column equilibration. The mobile phase from the first 2 min of each analysis was diverted to the waste in order to protect the MS ionization source from the early eluting matrix components. Between injections the autosampler was sequentially rinsed with 1000 μ L of H₂O/CH₃OH, 80/20 v/v and H₂O/CH₃OH, 20/80 v/v to remove any sample residuals.

Precursor ion full scan spectra of the studied protein was acquired in positive ionization mode (m/z range 50–1800) using a direct infusion of an insulin solution (1 μ g/mL in 0.1% FA) using a syringe pump operating at a flow rate of 5 μ L/min. Stable and reproducible response was observed in (+) mode corresponding to its protonated ion [M+5H]⁵⁺ (1162.2 m/z); thus, it was used as quantitation ion. The electrospray source block and the desolvation temperatures were 120 and 400 °C, respectively. The capillary and the cone voltage were 3 kV and 30 V, respectively. Nitrogen was utilized as both desolvation and nebulizing gas operated at 600 and 50 L min⁻¹. A dwell time of 25 ms was used. The operation of the LC-MS system and the data acquisition were carried out using MassLynx v. 4.1 software.

A linear calibration curve was constructed using six calibration levels in the range of 0.10–5.2 μ g/mL. A weighted factor of 1/X was selected to minimize the deviation of the back-calculated values (residuals) from the theoretical concentrations. The correlation coefficient (r) of 0.9902 demonstrating satisfactory linearity in the studied concentration range. The lower quantifiable concentration of 0.1 μ g/mL was taken as LLOQ and the % RSD of three replicate injections of standard solution was less than 2.0%.

2.11. Statistical analysis

The results for the diffusion studies are presented as mean \pm standard deviation of three experiments. Statistical differences were tested using unpaired Student t -test ($p < 0.05$).

3. Results and discussion

3.1. Design and fabrication of HMNs

HMNs were designed in CAD modeling with a height of 1000 μ m for curved pyramid and syringe-like configurations. The microneedles' interspacing was set at 2000 μ m (center to center distance) and the whole patch was a 15 \times 15 mm square. The designs of the 3D printed

HMNs of both geometries are presented in Fig. 2. Curved pyramid geometry was previously optimized in a previous work [36] and as such, array surface was kept constant and interspacing (center to center distance) was reduced at 2000 μ m resulting to a 6 \times 6 HMN array. This alteration aims to a reduction of insertion force and thus to an easier perforation of stratum corneum [37]. Syringe-like geometry was introduced for comparison reasons. Insertion forces and permeability values were compared, and conclusions were made on the suitability of the two geometries for drug administration. Interspacing and array surface designed values were common for both geometries. Some parameters namely layer height and curing time, were experimentally optimized. 3D printing angles were different for the two designs. The determination of the 3D printing angle follows the logic that the HMN surface containing the channel projection must be parallel to the building platform. In this way clogging of microchannels is prevented [38]. Hence, 3D printing angle of curved pyramid geometry was 52.63°, while for syringe-like printing angle was 36.25°. The reservoirs were common for both the curved pyramid and syringe-like HMNs. HMNs and reservoirs were not simultaneously 3D printed resulting in order to avoid a severe increase of 3D printing time. Therefore, reservoirs were separately 3D printed with a 100 μ m layer resolution compared to the highly detailed HMNs. The dimensions of the final device were 16 \times 18 mm (length \times width \times height).

Fig. 3 a - d depict SEM images of HMNs of both geometries. The height of curved pyramid HMNs was measured to be 900 μ m \pm 40 μ m, while lateral tip length was found to be 40–55 μ m. For syringe-like HMNs height was 955 μ m \pm 40 μ m. Lateral tip length varied in the same range, while tip shape was quite oblong. Both tips were sharp enough ensuring the success of perforation process. Microchannel projected area of syringe-like HMNs was much larger compared to the corresponding of curved HMNs, as can be estimated in Fig. 3b. LCD printed HMNs are coarse compared to conventional non printed microneedles, while their lateral tip length cannot be less than \sim 50 μ m. This is a limitation method associated with printing procedure. As a result, skin penetration may be achieved in higher forces. Yet, insertion forces were kept at tolerable values (see section 3.4).

Regarding the geometry that can be achieved while 3D printing HMNs, it should be noted that the successful formation of microchannels requires the existence of an inclined microneedle surface which contains the ending of the channel in the form of ellipsis [38]. As a result, any geometry that fulfills this requirement and can yield sharp tipped microneedles is considered suitable. Two common 3D printed geometries are beveled and triangular pyramid [28,31]. Of great significance is the fact that inclined surfaces should be parallel to building platform in order to ensure well forming of microchannels (no clogs). Table 1 summarizes some conditions under which successful printing of HMNs is

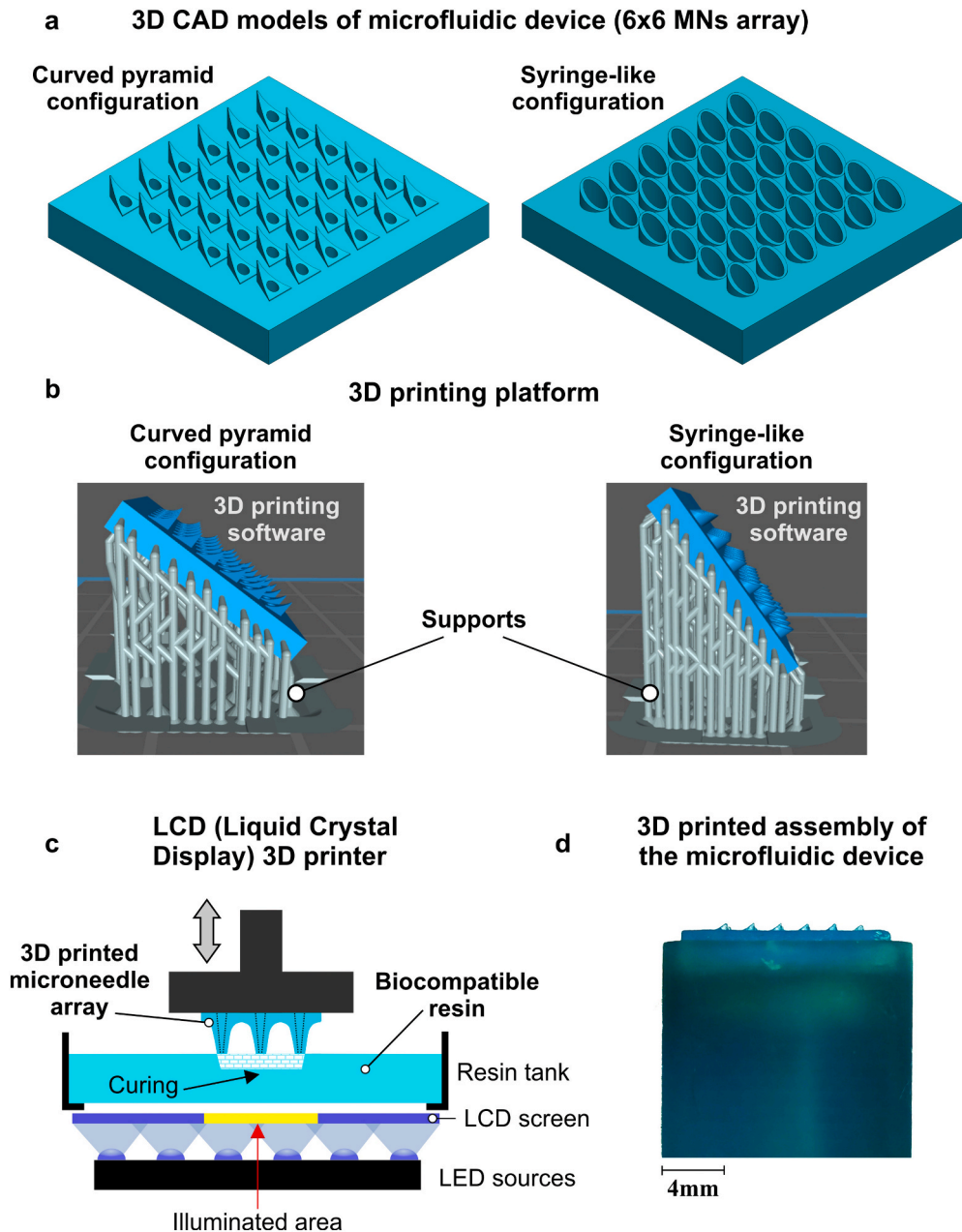


Fig. 2. (a) 3D CAD models of microfluidic device (b) 3D platforms (curved pyramid and syringe-like configurations), (c) Schematic representation of the vat polymerization 3D printer for the fabrication of the HMN arrays and reservoirs and (d) the 3D printed microneedle arrays fitted in a reservoir adapter suitable for drug administration.

avored or not. Hexagon, square pyramid and beveled geometry are included. Importance of inclined surface along with printing angle is raised [38].

NextDent Ortho Rigid printing material is a Class IIa biocompatible resin according to the manufacturer. Hence, it complies with ISO-10993-1 which means that printed material is not expected to exert systemic or topical adverse effects [39]. Despite this certification, there should be awareness as the possibility of unpolymerized monomer leaching may exist, depending on the physicochemical properties of the resin [40]. To encounter this possibility, a prime action is to reassure an effective polymerization in terms of time curing [41]. In addition, alcohol rinsing of the printed objects has been referred to improve their biocompatibility probably because of the massive removal of monomers [42]. Furthermore, coating addition prevents leaching because it poses a barrier and at least adds a lag time to monomer mitigation [43].

Nevertheless, the possibility of toxicity due to monomer leaching was experimentally assessed in a previous work of us. Briefly, PBS extracts of 3D-printed objects collected at different time-points were incubated with human adult low-calcium keratinocytes. According to experimental findings, growth inhibition may occur after a period of time; yet, cell death is not induced. Taking into consideration that the proposed polymer coated HMNs are purposed for a few minute drug administration, it is unlikely that cell/tissue viability will be affected [36].

3.2. μ CT studies

In this study we analyzed two different configurations; curved pyramid geometry patch and syringe-like geometry patch, both made of Nextdent Ortho Rigid resin. X-ray μ CT of the HMNs and their microchannels are illustrated in Fig. 4 a-h. The results of the analysis are

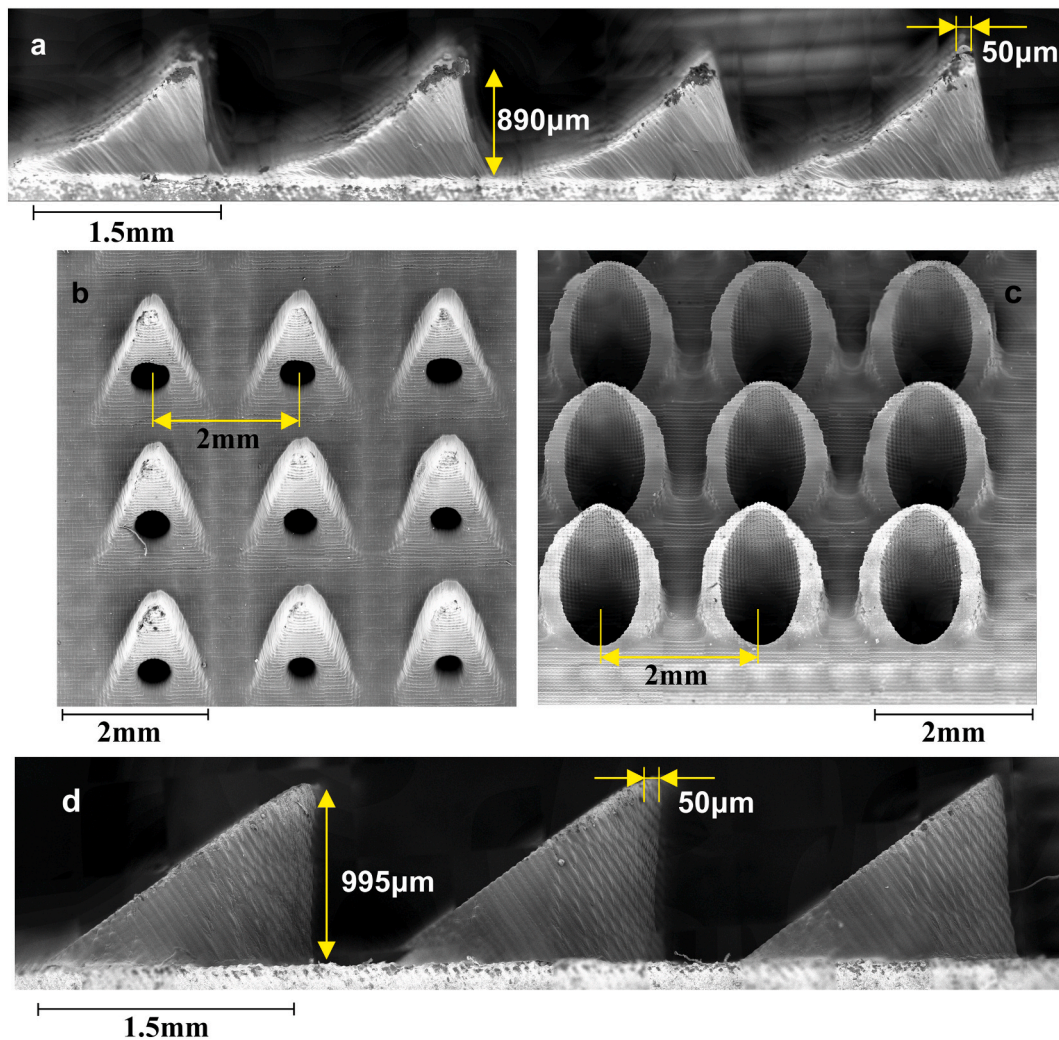


Fig. 3. SEM micrographs: (a), (b) 3D printed curved pyramid and (c), (d) 3D printed syringe-like HMN arrays.

Table 1

Summarized results of successful or not microchannel formation. All 3D-printings included 10s curing time, 400 $\mu\text{m/s}$ lifting speed and 30 μm layer height.

Geometry	Non-clogged microchannel	3D Printing Angles
Beveled	Yes	-45°
Beveled	No	0°, 90°, +45°
Hexagon	No	0°, 90°, +45°, -45°
square pyramid	No	0°, 90°, +45°, -45°

presented in Table 2, where it can be concluded that the 3D printing method allows for high consistency and reproducibility with respect to needles' length (quantified as *MaxZ-MinZ*). Needle length variation was <5% across the different needles of each patch, with the curved pyramid geometry performing better than the needle-like ones. Mean needle length was found to be ~ 0.856 mm for the curved pyramid geometry and 0.955 for the syringe-like. Volumetric reproducibility (*volume*) amongst needles of the same batch showed somewhat higher variation but still below 15%. Given that the shape variation, as assessed by both the *aspect ratio* and the *minimum ferret diameter* of these objects, is in the order of $\sim 3\text{--}6\%$ for both geometries, one could argue that the excess variations seen in *volume* is due to surface finish/roughness. This is further supported by the *volume/surface area* measurements where variation is seen to be between 6 and 7%.

Reproducibility of the lumen seem to be comparable, with

volumetric variability (*volume*) ranging between ~ 8 and 17%. In this context, the *minimum ferret diameter* (a.k.a. minimum caliper diameter) can be used to assess the smaller internal cross-section of each lumen. It can be used to highlight obstructions and narrowings. The *average minimum ferret diameter* was ~ 0.6 mm for curved pyramid geometry, while the syringe-like geometry exhibited a much greater *minimum ferret diameter* of 0.9 mm. The syringe-like geometry performed better in terms of lumen consistency. No serious obstructions or narrowings were observed in any of the 32 needle-plus-lumen composite objects.

3.3. Contact angle studies

Printing films at a different angles results in a different roughness on their surface, due to the fact that slicing gives different surface areas. Hence, contact angle varied according to printing angles. As seen in Fig. 5, as printing angle increases from 36.25° to 52.63° contact angle between water drops and substrates decreases (control 36.25° vs control 52.63°, coated at 36.25° vs coated at 52.63°). Furthermore, the addition of the polymer on the substrates on both printing angles causes reduction of the contact angle by nearly 40°, reaching values of 22° and 15° at equilibrium for 36.25° and 52.63° printing angles respectively. The significant decrease of contact angle between the substrate and water favors the flow of water-based solutions and as such, polymer addition was successful. Moreover, water rinsed coated films (36.25°) presented equal contact angles at equilibrium indicating similar wetting behavior of the coated microneedles after rinsing.

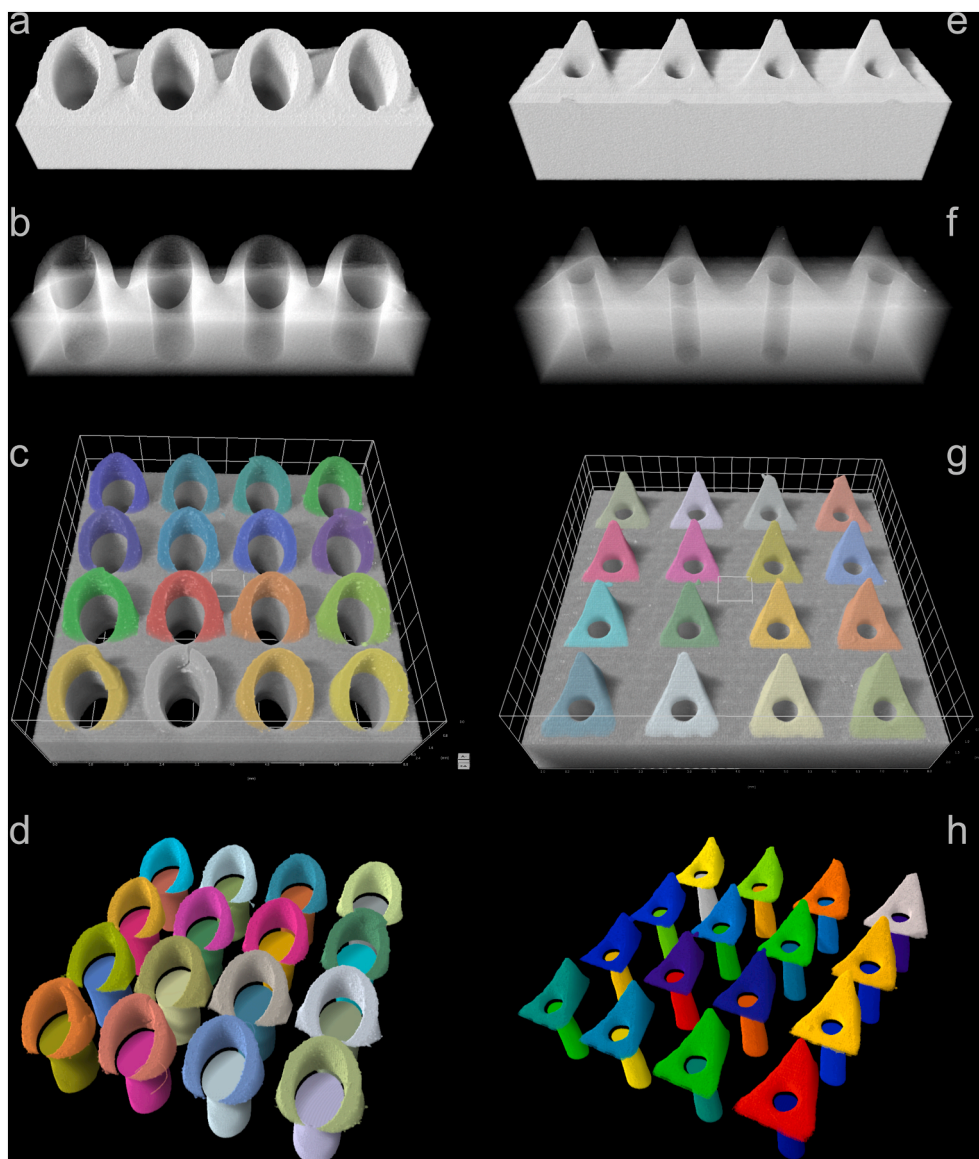


Fig. 4. X-ray μ CT of curved pyramid, syringe-like HMNs and their microchannels. Volumetric (a), (e) and semitransparent (b), (f) virtual section of a single needle row showing the needle structure and the lumen with respect to the needle. Sub-panels (c), (d) and (g), (h) show the segmented individual needles (c), (g) and the needle/lumen models (d), (h) used for the volumetric quantification of the structures presented in Table 2. Grid-size 0.8 mm and 0.5 mm in (c) and (g) respectively.

during the few minute drug administration should be considered negligible as regards the wetting behavior of the microneedles. Contact angle measurements at different positions of the same sample resulted into contact angle differences of below 1.5° . Taking into account the roughness of the structures surface such small differences reflect the homogeneous structuring and coating of the surface.



3.4. Mechanical characterization

Compression tests were conducted using forces up to 416.5 N for curved pyramid HMNs and 650 N for syringe-like HMNs, which in fact is much greater force than this HMN arrays will experience during insertion into the skin. After experiments HMN arrays were examined with SEM, revealing the extension of the damage that has happened. As shown in Fig. 6 a-e, both curved pyramid and syringe-like geometries experienced an extreme stress condition at 416.5 N and 650 N, respectively. Fig. 6a shows force-displacement curve, where can be seen that syringe-like HMNs can withstand forces up to 650 N, but after that they are more heavily damaged. As shown in Fig. 6a, fracture was observed at

416.5 N for curved pyramid microneedle array. Compression failure test results of the curved pyramid and syringe-like HMNs in Fig. 6a reveal that the failure strength was 12 N per HMN and 18 N per HMN, respectively. Cracks, partial detachments and shape alterations were observed. Whereas complete fracture of curved pyramid HMNs was not achieved as shown in Fig. 6c and e, results were not the same for syringe-like HMNs. As seen in Fig. 6b and d, syringe-like HMNs experienced extreme damage with several parts of microneedle walls being lost, while one case of complete destruction was recorded. Material compression led to a 15% height loss in curved pyramid HMN geometry.

An indirect comparison could be made between the proposed curved pyramid HMNs and the pyramid coated microneedles manufactured by Douroumis et al. [32]. Both kinds of microneedles have similarities regarding their geometry and their material (similar components and mechanical characteristics). Given these facts, it is observed that coated pyramid microneedles [32] start to fail after applying a 457 N uniaxial load, while in the current study failure is recorded at lower forces (416.5 N) for curved pyramid HMNs, as it has been already mentioned. This comparison indicates that the lumen existence weakens mechanical

Table 2
Selected metrics of curved pyramid and syringe-like 3D printed hollow microneedles.

Geometry Composition	curved pyramid		syringe-like	
	mean ± SD ^a [coef.var]	Lumen n = 16	Needles n = 16	Lumen n = 16
Segmented objects				
Selected metrics				
Volume (mm ³)	0.284 ± 0.037 [13.1%]	0.354 ± 0.061 [17.3%]	0.45 ± 0.055 [12.26%]	1.243 ± 0.105 [8.44%]
Volume/Surface Area (mm)	0.069 ± 0.006 [5.97%]	0.113 ± 0.009 [7.67%]	0.071 ± 0.005 [7.4%]	0.184 ± 0.008 [4.11%]
Max Z - Min Z (mm)	0.858 ± 0.024 [2.83%]	n/a	0.955 ± 0.039 [4.11%]	n/a
Aspect Ratio	0.439 ± 0.015 [3.47%]	0.19 ± 0.028 [14.75%]	0.433 ± 0.027 [6.24%]	0.5 ± 0.024 [4.76%]
Min Feret Diameter (mm)	0.858 ± 0.024 [2.83%]	0.622 ± 0.068 [10.89%]	0.955 ± 0.039 [4.11%]	0.976 ± 0.026 [2.7%]

^a SD: standard deviation.

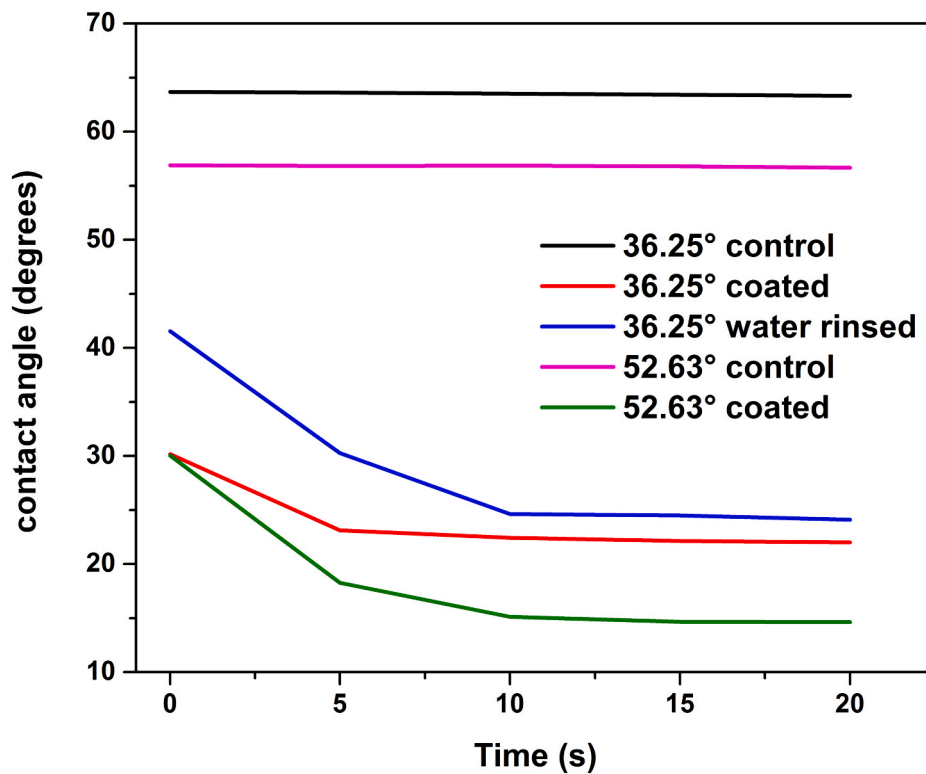


Fig. 5. Contact angle measurements as a function of time. Black and purple line: control films printed at 36.25° and 52.63° respectively. Red and blue line: coated and water rinsed films printed at 36.25°. Green line: coated film printed at 52.63°. (For interpretation of the references to colour in this figure legend, the reader is referred to the Web version of this article.)

strength of the pyramid-like microneedles, probably due to lateral wall thickness reduction, implying that the larger the lumen, the lower the mechanical strength. In addition, during the manufacturing procedure of the curved pyramid HMNs, it was observed that very large sized microchannels led to unsuccessful printings due to lateral wall thinning. Experimentally it was proved that 500 μm microchannel diameter does not compromise mechanical strength significantly while microchannels are very well formed.

On the other hand, the syringe-like configuration that has been studied in this work can withstand a force of 650 N with a microchannel

diameter of over 500 μm, indicating the significance of the geometry of the HMNs during the design process.

3.5. Skin penetration test

The capability of the HMNs to perforate SC, the applied forces and the comparison between two different geometrical configurations of HMNs have been investigated through instrumented penetration tests, supported by FEA simulations. FEA models have been introduced in order to improve the calculation accuracy of forces that have been

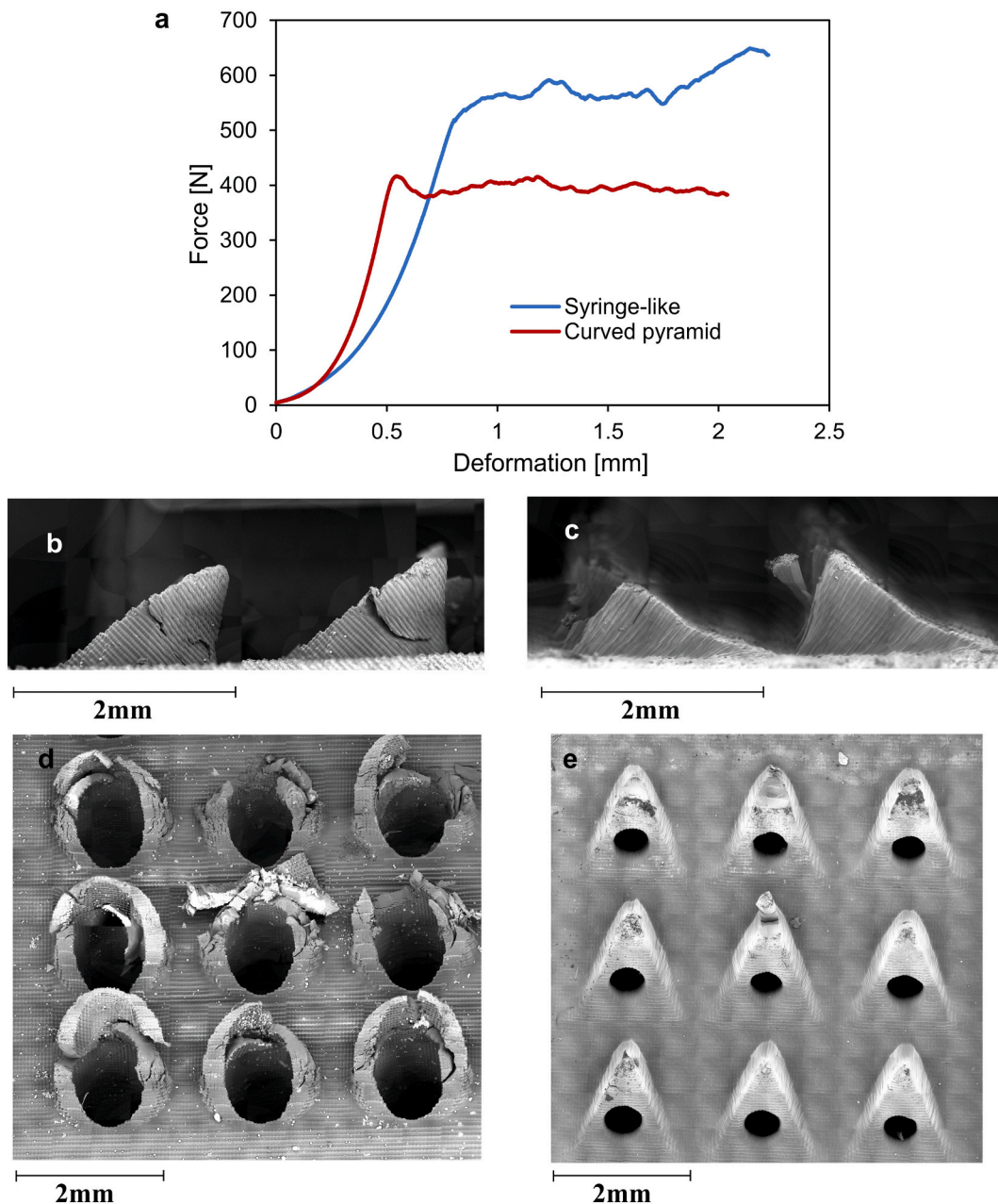


Fig. 6. (a) Failure tests demonstrating force-displacement experimental data, (b), (c), (d) and (d) SEM imaging of the curved pyramid and syringe-like HMN configuration after compression test.

applied during human skin penetration tests. An explicit dynamics analysis was performed on ANSYS code in order to investigate the insertion process of 3D printed HMN arrays into human skin. A multi-layered skin model consisting of three layers, SC, dermis and hypodermis, has been reported to be rather appropriate [44]. These works demonstrated that the skin deformation during the insertion process, as well as the insertion force of the microneedle for perforating the skin surface, accurately fitted the experimental data. In the current study, the experimental force-penetration depth data converged with the employed FE model simulating the insertion of two different 6×6 HMNs into human skin. The material properties needed for the FE model were measured for the resin used to fabricate the HMNs. The compressive strength of the NextDent 3D-printed resin was determined to be 135 ± 5 MPa and the elastic modulus 1400 MPa, according to compression and nanoindentation mechanical testing techniques [45–47].

A schematic representation of the FEA model is illustrated in Fig. 7a,

where the two different configurations of HMN arrays are clearly demonstrated, along with the boundary conditions and the three layers of the skin. These three layers are equivalent to the main skin layers. More specifically, the first layer represents SC and has been given a thickness of $h_1 = 20 \mu\text{m}$, the second layer is equivalent to the dermis where $h_2 = 1.5$ mm and the third layer to the hypodermis where $h_3 = 1.0$ mm. Material failure and an evolving contact surface between HMNs and target was introduced, in order to define the insertion of the HMN array and the surface of the skin, which is governed by large deformations. A material erosion algorithm was utilized to study the failure and separation of the material. The material erosion method removes distorted elements during the solution, i.e. along the HMN trajectory, based upon material failure and separation due to fracturing of the surface of the skin. Since the hypodermis layer is not involved with failure and significant deformation, it was assumed to be simulated as elastic material, while the first two layers, SC and dermis, were

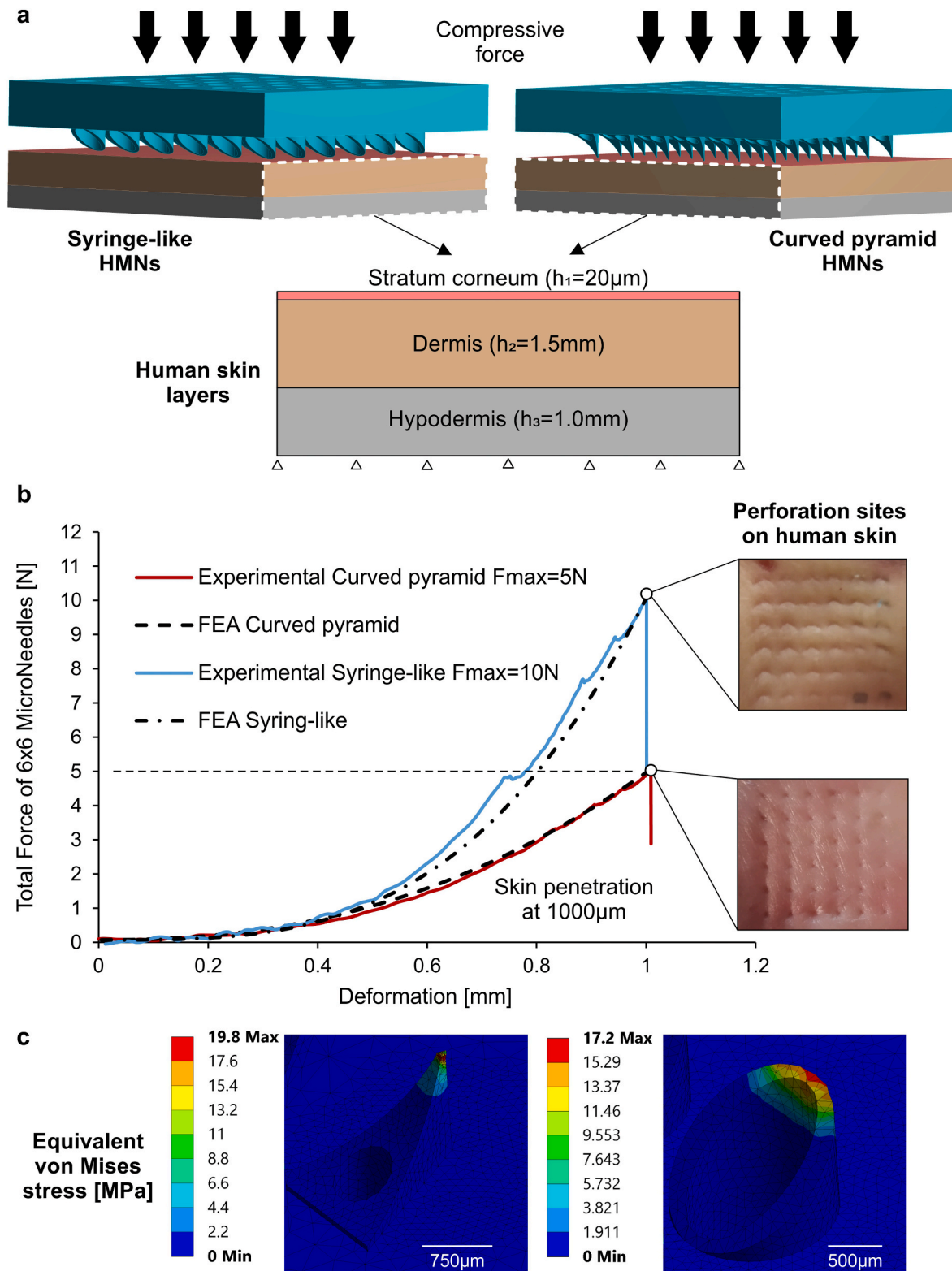


Fig. 7. Penetration tests using the curved pyramid and syringe-like HMNs: (a) schematic representation of FEA simulation, (b) insertion force-deformation curve-fitted by FEA along with the perforation sites on human skin and (c) stress distribution of curved pyramid and syringe-like HMNs at the last step of the simulation of skin penetration using FEA.

modeled as hyperelastic material.

The initial values of the mechanical properties of the SC, the dermis and the hypodermis assumed in these simulations were acquired by previous work and literature [44,48]. The material parameters were defined by fitting the FEA force-depth with the experimental data. Thus,

the identification procedure could be considered as a minimization problem. A Neo-Hookean material model was considered very efficient in a previous work [44], so its model parameters (C_{10} , K) were explored in order to minimize the difference between the computationally generated force-displacement curves and the experimental penetration

test data. Therefore, the skin properties for SC were determined as $C_{10} = 0.12$ MPa, $K_{SC} = 5.0$ MPa, for dermis: $C_{10} = 1.0$ MPa, $K_D = 25$ MPa and an elastic behavior was considered for the equivalent hypodermis layer with Poisson's ratio of 0.48 and Young's modulus of 3.8×10^4 Pa. The insertion speed of the HMN array into the skin layers was set constant at 0.5 mm/min.

During penetration testing, the HMNs were pressed into human skin with forces applied up to 5 N for curved pyramid HMNs and 10 N for syringe-like HMNs. Fig. 7b demonstrates the results of penetration tests along with superimposed skin images confirming perforation of SC. Curved pyramid HMNs are capable of perforating human skin at 5 N. Perforation occurred for at least 33 out of 36 HMNs. However, perforation for syringe-like geometry occurs at 10 N (at least 30 out of 36 HMNs). This can be explained by the more refined tip area of the curved pyramid geometry. In addition, as mentioned above, the tip of syringe-like HMNs is quite oblong, which in fact spreads the concentrated energy in a greater skin area. As a result, force causing perforation is doubled. More specifically, the insertion force was calculated to be 5.03 N, i.e. $5.02/36 = 0.14$ N per curved pyramid microneedle. The ultimate insertion force for perforation of SC was calculated to be 10.07 N, i.e. $10.07/36 = 0.28$ N per microneedle regarding the syringe-like configuration. These values are significantly below the ultimate strength of curved pyramid and syringe-like geometries, i.e. 12 N per HMN and 18 N per HMN, as mentioned previously in the compression failure tests. Taking into consideration that both HMN geometries can withstand axial forces of more than 400 N, it can be estimated that safety factor (SF), which is defined as the ratio fracture force/insertion force, is much greater than 1. This eliminates the risk of in-skin HMN fracturing and ensures safe skin application. Therefore, this confirms that both curved pyramid and syringe-like HMNs are appropriate for on-body

applications. In addition, insertion forces of 5 N and 10 N, although greater than other forces referred in literature, are considered satisfyingly low for human tolerability. According to literature, these forces correspond to a gentle push of HMNs on skin enabling at the same time self-administration of drugs [49]. Hence, it is not expected that patient compliance will be significantly affected.

The force-displacement responses for the HMN configurations are demonstrated in Fig. 7b. The results of simulations are shown in Fig. 7b and accurately curve-fitted the experimental force-deformation data up to maximum forces of 5 N and 10 N. During the deformation phase, the force exponentially increases as each of the HMNs is pressed against the skin. The drops in the experimental force-deformation curve may be explained by local perforation of single HMNs. Since the assumptions on the material parameters in the FEA model returned results that fitted the experimental data, the hyperelastic and elastic material model parameters of the skin were considered optimal. The simulation of the penetration test revealed that the stress concentration was located at the tip of the HMNs, as displayed by the equivalent von Mises stress results in Fig. 7c. This demonstrates the stress contouring of the FEA simulating the behavior of the HMN at the last step of the penetration test simulation. The maximum stress experienced by the insertion process was calculated to be 19.8 MPa and 17.2 MPa for the curved pyramid and syringe-like configuration, respectively. There is no concern regarding the concentration of the stress obtained at the tip area of the HMN for both the configurations, since the ultimate compressive strength was measured 135 ± 5 MPa, as mentioned previously.

SEM imaging of stratum corneum reveals the perforation sites caused by the HMNs. It is noted that each HMN geometry causes apertures of specific formation. Curved pyramid HMNs led to triangular shaped, while syringe-like HMNs led to oblong and half-ellipsoid apertures,

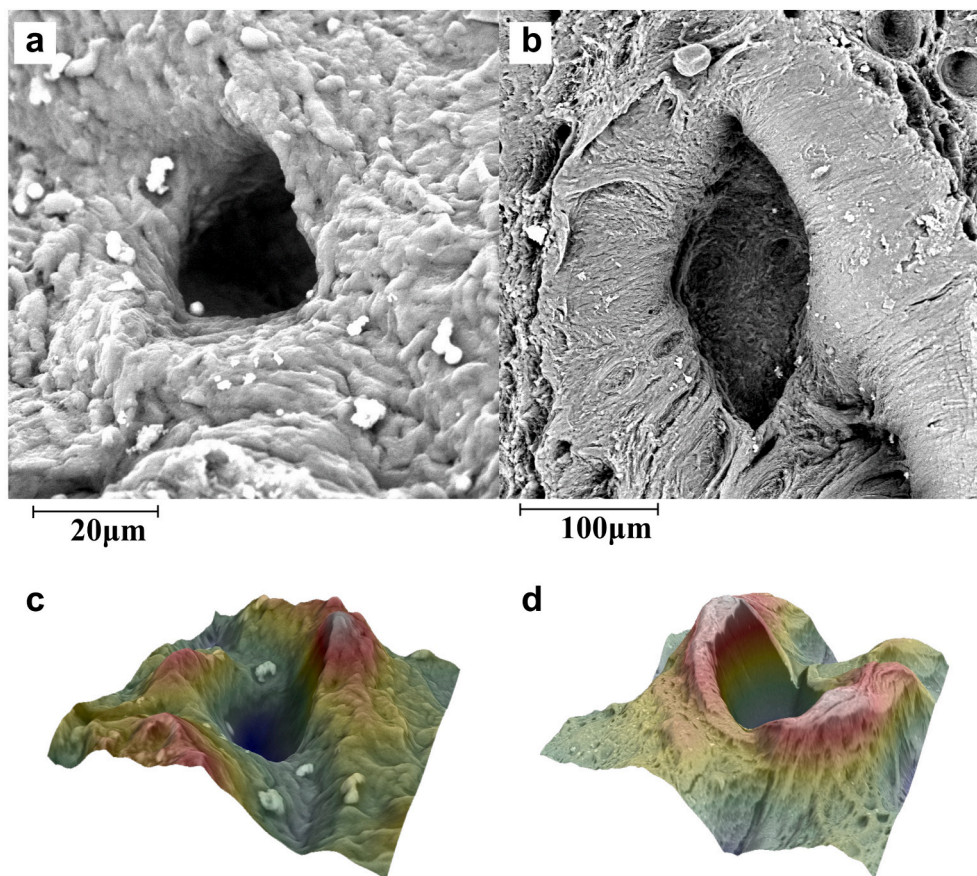


Fig. 8. SEM imaging of microneedle created perforation sites for (a) curved pyramid HMNs (b) syringe-like HMNs and 3D roughness reconstruction of perforation sites for (c) curved pyramid HMNs (d) syringe-like HMNs.

according to tip shape in each case. The pores created on skin surface after microneedle application is illustrated at Fig. 8a and b for curve-pyramid and syringe-like HMNs respectively. The 3D roughness reconstruction of perforation site for curved pyramid HMNs and syringe-like HMNs are illustrated in Fig. 8c and d.

3.6. Diffusion studies

The interactions between the coated surface of the microneedles and insulin at the timescale of 2 min (application time) are shown in Fig. 9a. The initial insulin concentration which was determined at 1.91×10^7 mU/L, dropped to 1.87×10^7 mU/L corresponding to ca. 2% decrease which can be considered negligible. The effect of the temperature had no effect to the stability of insulin as shown in Fig. 9b.

The cumulative amount of insulin permeated across human skin *in vitro* after 60 min is shown in Fig. 9c. The cumulative amount of insulin permeated upon application of curved pyramid microneedles and syringe-like microneedles was $4.3 \pm 1.1\%$ and $6.0 \pm 2.3\%$, respectively. Although there is no statistical difference (*t*-test, $p > 0.05$) between the cumulative amount insulin permeated across the skin using different microneedle patches the higher values obtained for the syringe-like HMNs might be attributed to the fact that microchannel formations are closely located to the tip enabling the transport of the macromolecule immediately within deeper skin. On the contrary in the case of the curved-pyramid HMNs the lower values obtained might be a combination of two factors. Firstly, the lower volume of their lumen (0.354 mm^3)

compared to that of syringe-like microneedles (1.243 mm^3) (Table 2) with the later allowing larger volumes to reach and penetrate the skin tissue Secondly, the microchannels in curved-pyramid microneedles are more distant from the skin surface resulting in slower permeation of peptide across the skin membrane. The low amount of insulin obtained in the current study might be attributed to the fact that full thickness skin (ca.1 mm) was used for the permeability studies. Skin permeation studies using laboratory animals reported significantly higher values compared to human skin [50]. Finally, the results obtained in the current study emphasize the necessity of an applicator which will diminish large fluctuations to transported amount of the peptide across the skin due to handling constraints.

4. Conclusions

In the current study the structural features of two different 3D printed 6×6 HMN geometries were assessed. Non-destructive 3D (volumetric) imaging by means of μ CT demonstrated that the 3D printing method used in this study allows for high consistency and reproducibility with respect to needles' geometric characteristics. Both geometries were able to withstand extreme axial forces ($>400 \text{ N}$), while skin penetration occurred at 5 N for curved-pyramid and at 10 N for syringe-like geometry, resulting in high safety factor. These results converged with the corresponding from FEA simulations. Diffusion studies demonstrated that syringe-like HMNs were more effective upon insulin administration compared with curved pyramid ones. Although

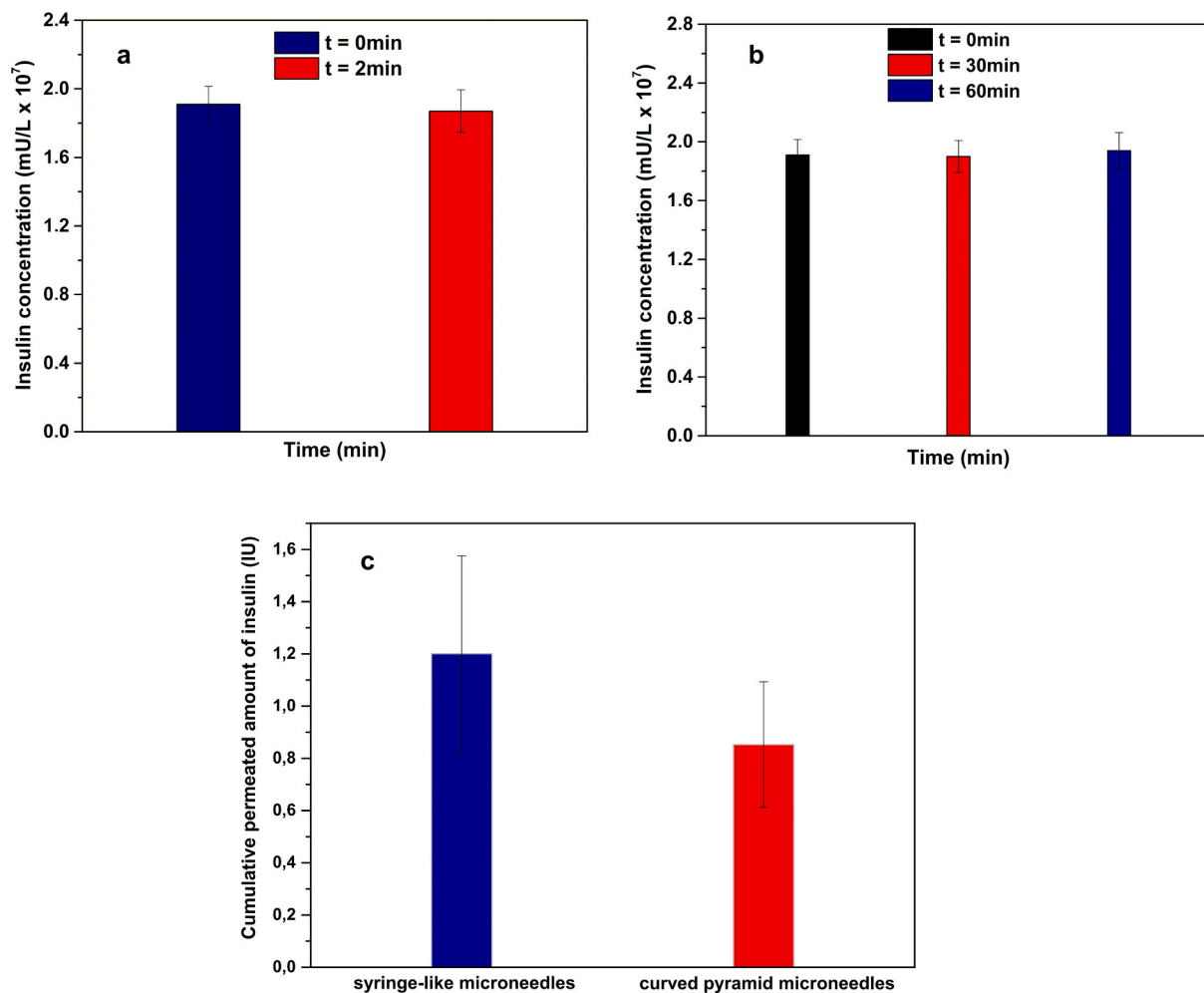


Fig. 9. (a) Binding studies of insulin to surfactant coated microneedles ($n = 3$), (b) stability studies of insulin at $37 \text{ }^\circ\text{C}$ ($n = 3$) and (c) cumulative amount of insulin permeating human skin after HMN treatment.

syringe-like geometry penetrates skin at higher insertion force, it is probably more suitable for macromolecular drug delivery which might be attributed to the geometrical characteristics of the microneedles. The relatively low amount of transported insulin across human skin *in vitro* might be attributed to the selected type of skin membrane (human skin) and the thickness of the membrane.

CRedit roles

Conceptualization DT DGF; Data curation IX, KT; Formal analysis IX, KT; Funding acquisition DGF; Investigation IX, KT, DT, ED, OLK, CKZ, EKT, EK, D.G, DGF; Methodology IX, KT, EKT, CKZ; Project administration DT, DGF; Resources DGF; Software DT; Supervision DGF; Validation IX, KT, DGF, DT; Visualization EKT, OLK; Roles/Writing - original draft IX, KT; Writing - review & editing DT, DGF.

Declaration of competing interest

The authors declare that they have no known competing financial interests or personal relationships that could have appeared to influence the work reported in this paper.

Acknowledgements

This research is co-financed by Greece and the European Union (European Social Fund - ESF) through the operational program "Human Resources Development, Education and Lifelong Learning 2014–2020" in the context of the project "Fabrication of 3D printed microneedles for transdermal personalized delivery of insulin" (MIS 5047927). We also acknowledge the μ -VIS X-Ray Imaging Centre at the University of Southampton and Wellcome Trust Biomedical Resource and Technology Development Grant 212940/Z/18/Z for supporting the tomographic imaging studies.

References

- P. Khanna, J.A. Strom, J.I. Malone, S. Bhansali, Microneedle-based automated therapy for diabetes mellitus, *J. Diabetes Sci. Technol.* 2 (2008) 1122–1129, <https://doi.org/10.1177/193229680800200621>.
- B.A. Jana, A.D. Wadhvani, Microneedle - future prospect for efficient drug delivery in diabetes management, *Indian J. Pharmacol.* 51 (2019) 4–10, https://doi.org/10.4103/ijp.IJP_16_18.
- R. Singh, S. Singh, J.W. Lillard, Past, present, and future technologies for oral delivery of therapeutic proteins, *J. Pharmaceut. Sci.* 97 (2008) 2497–2523, <https://doi.org/10.1002/jps.21183>.
- H.S. Gill, M.R. Prausnitz, Does needle size matter? *J. Diabetes Sci. Technol.* 1 (2007) 725–729, <https://doi.org/10.1177/193229680700100517>.
- J. Swaminathan, C. Ehrhardt, Liposomal delivery of proteins and peptides, *Expert Opin. Drug Deliv.* 9 (2012) 1489–1503, <https://doi.org/10.1517/17425247.2012.735658>.
- G. Jiang, B. Xu, J. Zhu, Y. Zhang, T. Liu, G. Song, Polymer microneedles integrated with glucose-responsive mesoporous bioactive glass nanoparticles for transdermal delivery of insulin, *Biomed. Phys. Eng. Express.* 5 (2019), 045038, <https://doi.org/10.1088/2057-1976/ab3202>.
- I. Lindmayer, K. Menassa, J. Lambert, A. Moghrabi, L. Legendre, C. Legault, M. Letendre, J.P. Hallé, Development of new jet injector for insulin therapy, *Diabetes Care* 9 (1986) 294–297, <https://doi.org/10.1089/dia.2011.0077>.
- K. Tachibana, Transdermal delivery of insulin to alloxan-diabetic rabbits by ultrasound exposure, *Pharm. Res. (N. Y.)* 9 (1992) 952–954, <https://doi.org/10.1023/A:1015869420159>.
- T.W. Wong, T.Y. Chen, C.C. Huang, J.C. Tsai, S.W. Hui, Painless skin electroporation as a novel way for insulin delivery, *Diabetes Technol. Therapeut.* 13 (2011) 929–935, <https://doi.org/10.1089/dia.2011.0077>.
- O. Pillai, V. Nair, R. Panchagnula, Transdermal iontophoresis of insulin: IV. Influence of chemical enhancers, *Int. J. Pharm.* 269 (2004) 109–120, <https://doi.org/10.1016/j.ijpharm.2003.09.032>.
- T. Waghule, G. Singhvi, S.K. Dubey, M.M. Pandey, G. Gupta, M. Singh, K. Dua, Microneedles: a smart approach and increasing potential for transdermal drug delivery system, *Biomed. Pharmacother.* 109 (2019) 1249–1258, <https://doi.org/10.1016/j.biopha.2018.10.078>.
- M.R. Prausnitz, Engineering microneedle patches for vaccination and drug delivery to skin, *Annu. Rev. Chem. Biomol. Eng.* 8 (2017) 177–200, <https://doi.org/10.1146/annurev-chembioeng-060816-101514>.
- S.P. Davis, W. Martanto, M.G. Allen, M.R. Prausnitz, Hollow metal microneedles for insulin delivery to diabetic rats, *IEEE Trans. Biomed. Eng.* 52 (2005) 909–915, <https://doi.org/10.1109/TBME.2005.845240>.
- J. Gupta, E.L. Felner, M.R. Prausnitz, Minimally invasive insulin delivery in subjects with type 1 diabetes using hollow microneedles, *Diabetes Technol. Therapeut.* 11 (2009) 329–337, <https://doi.org/10.1089/dia.2008.0103>.
- N. Roxhed, B. Samel, L. Nordquist, P. Griss, G. Stemme, Painless drug delivery through microneedle-based transdermal patches featuring active infusion, *IEEE Trans. Biomed. Eng.* 55 (2008) 1063–1071, <https://doi.org/10.1109/TBME.2007.906492>.
- P.M. Wang, M. Cornwell, J. Hill, M.R. Prausnitz, Precise microinjection into skin using hollow microneedles, *J. Invest. Dermatol.* 126 (2006) 1080–1087, <https://doi.org/10.1038/sj.sjid.5700150>.
- J.J. Norman, M.R. Brown, N.A. Raviello, M.R. Prausnitz, E.I. Felner, Faster pharmacokinetics and increased patient acceptance of intradermal insulin delivery using a single hollow microneedle in children and adolescents with type 1 diabetes, *Pediatr. Diabetes* 14 (2013) 459–465, <https://doi.org/10.1111/pedi.12031>.
- A. Doraiswamy, C. Jin, R.J. Narayan, P. Mageswaran, P. Mente, R. Modi, R. Auyeung, D.B. Chrisey, A. Ovsianikov, B. Chichkov, Two photon induced polymerization of organic-inorganic hybrid biomaterials for microstructured medical devices, *Acta Biomater.* 2 (2006) 267–275, <https://doi.org/10.1016/j.actbio.2006.01.004>.
- A. Ovsianikov, B. Chichkov, P. Mente, N.A. Monteiro-Riviere, A. Doraiswamy, R. J. Narayan, Two photon polymerization of Polymer?Ceramic hybrid materials for transdermal drug delivery, *Int. J. Appl. Ceram. Technol.* 4 (2007) 22–29, <https://doi.org/10.1111/j.1744-7402.2007.02115.x>.
- S.D. Gittard, A. Ovsianikov, B.N. Chichkov, A. Doraiswamy, R.J. Narayan, Two-photon polymerization of microneedles for transdermal drug delivery, *Expert Opin. Drug Deliv.* 7 (2010) 513–533, <https://doi.org/10.1517/17425241003628171>.
- A. Trautmann, G.L. Roth, B. Nujiqi, T. Walther, R. Hellmann, Towards a versatile point-of-care system combining femtosecond laser generated microfluidic channels and direct laser written microneedle arrays, *Microsyst. Nanoeng.* 5 (2019), <https://doi.org/10.1038/s41378-019-0046-5>.
- C. Liao, W. Anderson, F. Antaw, M. Trau, Two-Photon nanolithography of tailored hollow three-dimensional microdevices for biosystems, *ACS Omega* 4 (2019) 1401–1409, <https://doi.org/10.1021/acsomega.8b03164>.
- K. Moussi, A. Bukhamsin, T. Hidalgo, J. Kosel, Biocompatible 3D printed microneedles for transdermal, intradermal, and percutaneous applications, *Adv. Eng. Mater.* 22 (2020) 1901358, <https://doi.org/10.1002/adem.201901358>.
- B. Szeto, A. Aksit, C. Valentini, M. Yu, E.G. Werth, S. Goeta, C. Tang, L.M. Brown, E.S. Olson, J.W. Kysar, A.K. Lalwani, Novel 3D-printed hollow microneedles facilitate safe, reliable, and informative sampling of perilymph from Guinea pigs, *Hear. Res.* 400 (2021), <https://doi.org/10.1016/j.heares.2020.108141>.
- J.F. Xing, M.L. Zheng, X.M. Duan, Two-photon polymerization microfabrication of hydrogels: an advanced 3D printing technology for tissue engineering and drug delivery, *Chem. Soc. Rev.* 44 (2015) 5031–5039, <https://doi.org/10.1039/c5cs00278h>.
- C. Farias, R. Lyman, C. Hemingway, H. Chau, A. Mahacek, E. Bouzos, M. Mobed-Miremedi, Three-dimensional (3D) printed microneedles for microencapsulated cell extrusion, *Bioengineering* 5 (2018), <https://doi.org/10.3390/bioengineering5030059>.
- C. Yeung, S. Chen, B. King, H. Lin, K. King, F. Akhtar, G. Diaz, B. Wang, J. Zhu, W. Sun, A. Khademhosseini, S. Emaminejad, A 3D-printed microfluidic-enabled hollow microneedle architecture for transdermal drug delivery, *Biomicrofluidics* 13 (2019), <https://doi.org/10.1063/1.5127778>.
- P.R. Miller, S.D. Gittard, T.L. Edwards, D.A.M. Lopez, X. Xiao, D.R. Wheeler, N. A. Monteiro-Riviere, S.M. Brozik, R. Polsky, R.J. Narayan, Integrated carbon fiber electrodes within hollow polymer microneedles for transdermal electrochemical sensing, *Biomicrofluidics* 5 (2011) 13415, <https://doi.org/10.1063/1.3569945>.
- H. Derakhshandeh, F. Aghabaglou, A. McCarthy, A. Mostafavi, C. Wiseman, Z. Bonick, I. Ghanavati, S. Harris, C. Kreikemeier-Bower, S.M. Moosavi Basri, J. Rosenbohm, R. Yang, P. Mostafalu, D. Orgill, A. Tamayol, A wirelessly controlled smart bandage with 3D-printed miniaturized needle arrays, *Adv. Funct. Mater.* 30 (2020) 1905544, <https://doi.org/10.1002/adfm.201905544>.
- M. Gieseke, V. Senz, M. Vehse, S. Fiedler, R. Irsig, M. Hustedt, K. Sternberg, C. Nölke, S. Kaierle, V. Wesling, J. Tiggesbäumker, K.H. Meiwes-Broer, H. Seitz, K. P. Schmitz, H. Haferkamp, Additive manufacturing of drug delivery systems, *Biomed. Technol.* 57 (2012) 398–401, <https://doi.org/10.1515/bmt-2012-4109>.
- S.N. Economidou, M.J. Uddin, M.J. Marques, D. Douroumis, W.T. Sow, H. Li, A. Reid, J.F.C. Windmill, A. Podoleanu, A novel 3D printed hollow microneedle microelectromechanical system for controlled, personalized transdermal drug delivery, *Addit. Manuf.* 38 (2021) 101815, <https://doi.org/10.1016/j.addma.2020.101815>.
- S.N. Economidou, C.P.P. Pere, A. Reid, M.J. Uddin, J.F.C. Windmill, D.A. Lamprou, D. Douroumis, 3D printed microneedle patches using stereolithography (SLA) for intradermal insulin delivery, *Mater. Sci. Eng. C. Mater. Biol. Appl.* 102 (2019) 743–755, <https://doi.org/10.1016/j.msec.2019.04.063>.
- H. Quan, T. Zhang, H. Xu, S. Luo, J. Nie, X. Zhu, Photo-curing 3D printing technique and its challenges, *Bioact. Mater.* 5 (2020) 110–115, <https://doi.org/10.1016/j.bioactmat.2019.12.003>.
- M. Wu, Y. Zhang, H. Huang, J. Li, H. Liu, Z. Guo, L. Xue, S. Liu, Y. Lei, Assisted 3D printing of microneedle patches for minimally invasive glucose control in diabetes, *Mater. Sci. Eng. C* 117 (2020) 111299, <https://doi.org/10.1016/j.msec.2020.111299>.
- O. Olatunji, D.B. Das, M.J. Garland, L. Belaid, R.F. Donnelly, Influence of array interspacing on the force required for successful microneedle skin penetration:

- theoretical and practical approaches, *J. Pharmaceut. Sci.* 102 (2013) 1209–1221, <https://doi.org/10.1002/jps.23439>.
- [36] I. Xenikakis, K. Tsongas, E.K. Tzintzimis, C.K. Zacharis, N. Theodoroula, E. P. Kalogianni, E. Demiri, I.S. Vizirianakis, D. Tzetzis, D.G. Fatouros, Fabrication of hollow microneedles using liquid crystal display (LCD) vat polymerization 3D printing technology for transdermal macromolecular delivery, *Int. J. Pharm.* 597 (2021), <https://doi.org/10.1016/j.ijpharm.2021.120303>.
- [37] J.S. Kochhar, T.C. Quek, W.J. Soon, J. Choi, S. Zou, L. Kang, Effect of microneedle geometry and supporting substrate on microneedle array penetration into skin, *J. Pharmaceut. Sci.* 102 (2013) 4100–4108, <https://doi.org/10.1002/jps.23724>.
- [38] I. Xenikakis, K. Tsongas, E.K. Tzintzimis, D. Tzetzis, D.G. Fatouros, Additive Manufacturing of hollow microneedles for insulin delivery, *Mod. Technol. Ind. Eng. Conf. Rom.* (2021) (in press).
- [39] B. NextDent, Netherlands. ((n.d)), <https://nextdent.com/products/ortho-rigid/>.
- [40] F. Alifui-Segbaya, J. Bowman, A.R. White, S. Varma, G.J. Lieschke, R. George, Toxicological assessment of additively manufactured methacrylates for medical devices in dentistry, *Acta Biomater.* 78 (2018) 64–77, <https://doi.org/10.1016/j.actbio.2018.08.007>.
- [41] D. Kim, J.-S. Shim, D. Lee, S.-H. Shin, N.-E. Nam, K.-H. Park, J.-S. Shim, J.-E. Kim, Effects of post-curing time on the mechanical and color properties of three-dimensional printed crown and bridge materials, *Polymers* 12 (2020) 2762, <https://doi.org/10.3390/polym12112762>.
- [42] M. Carve, D. Wlodkovic, 3D-printed chips: compatibility of additive manufacturing photopolymeric substrata with biological applications, *Micromachines* 9 (2018), <https://doi.org/10.3390/mi9020091>.
- [43] S. van den Driesche, F. Lucklum, F. Bunge, M.J. Vellekoop, 3D printing solutions for microfluidic chip-to-world connections, *Micromachines* 9 (2018), <https://doi.org/10.3390/mi9020071>.
- [44] I. Xenikakis, M. Tzintzimis, K. Tsongas, D. Andreadis, E. Demiri, D. Tzetzis, D. G. Fatouros, Fabrication and finite element analysis of stereolithographic 3D printed microneedles for transdermal delivery of model dyes across human skin in vitro, *Eur. J. Pharmaceut. Sci.* 137 (2019) 104976, <https://doi.org/10.1016/j.ejps.2019.104976>.
- [45] M. Mansour, K. Tsongas, D. Tzetzis, A. Antoniadis, Mechanical and dynamic behavior of fused filament fabrication 3D printed polyethylene terephthalate glycol reinforced with carbon fibers, *Polym. Plast. Technol. Eng.* 57 (2018) 1715–1725, <https://doi.org/10.1080/03602559.2017.1419490>.
- [46] D. Tzetzis, K. Tsongas, G. Mansour, Determination of the mechanical properties of epoxy silica nanocomposites through FEA-supported evaluation of ball indentation test results, *Mater. Res.* 20 (2017) 1571–1578, <https://doi.org/10.1590/1980-5373-MR-2017-0454>.
- [47] M. Mansour, K. Tsongas, D. Tzetzis, Measurement of the mechanical and dynamic properties of 3D printed polylactic acid reinforced with graphene, *Polym. Technol. Mater.* 58 (2019) 1234–1244, <https://doi.org/10.1080/03602559.2018.1542730>.
- [48] H.V. Tran, F. Charleux, M. Rachik, A. Ehrlicher, M.C. Ho Ba Tho, *In vivo* characterization of the mechanical properties of human skin derived from MRI and indentation techniques, *Comput. Methods Biomech. Biomed. Eng.* 10 (2007) 401–407, <https://doi.org/10.1080/10255840701550287>.
- [49] A. Kundu, T. Ausaf, S. Rajaraman, 3D printing, ink casting and micromachined lamination (3D PICL μ M): a makerspace approach to the fabrication of biological microdevices, *Micromachines* 9 (2018), <https://doi.org/10.3390/mi9020085>.
- [50] R.C. Wester, H.I. Maibach, *Animal models for transdermal delivery*, in: A. F. Kydonieus, B. Berner (Eds.), *Transdermal Deliv. Drugs*, CRC Press, Boca Raton, FL, 1987, pp. 61–70.